Article

A Wider Impedance Bandwidth Dual Filter Symmetrical MIMO Antenna for High-Speed Wideband Wireless Applications

Manish Sharma [1], Prem Chand Vashist [2], Ibrahim Alsukayti [3], Nitin Goyal [1], Divya Anand [4,5] and Amir H. Mosavi [6,*]

1   Chitkara University Institute of Engineering and Technology, Chitkara University, Rajpura 140401, India; manish.sharma@chitkara.edu.in (M.S.); nitin.goyal@chitkara.edu.in (N.G.)
2   Department of Information Technology, G.L. Bajaj Institute of Technology and Management, Greater Noida 201308, India; hod.it@glbitm.ac.in
3   Department of Computer Science, College of Computer, Qassim University, Buraydah 51452, Saudi Arabia; skiety@qu.edu.sa
4   School of Computer Science and Engineering, Lovely Professional University, Phagwara, Punjab 144411, India; divya.24844@lpu.co.in or divyaanand.y@gmail.com
5   Higher Polytechnic School, Universidad Europea del Atlántico, C/Isabel Torres 21, 39011 Santander, Spain
6   Institute of Software Design and Development, Obuda University, 1034 Budapest, Hungary
*   Correspondence: amir.mosavi@uni-obuda.hu

Abstract: This research article reports a compact fractal 4×4 UWB extended bandwidth MIMO antenna with physical dimensions of 44×44 mm^2 for high-speed wireless applications. The reported antenna comprises four fractal radiating elements that are symmetrical and placed orthogonal to each other with a respective rectangular ground printed on the opposite plane. A higher isolation is achieved between the radiating elements by the placement of a fractal patch orthogonally and no separate decoupling structure is required. The antenna offers a -10 dB transmission capacity of 2.84–15.88 GHz. The fractal radiating element, which is embedded by an inverted T-type stub placed within a rectangular slot and an etched rotated C-type slot, provides band-stop filters for WiMAX (Worldwide inter-operability for Microwave Access) and WLAN (wireless local area network)-interfering bands. The key parameters of diversity performance are compared by simulation and measurement (fabricated prototype) of ECC (envelope correlation coefficient), DG (directive gain), TARC (total active reflection coefficient) and CCL (channel capacity loss). The antenna offers an omnidirectional radiation pattern with an average gain of 3.52 dBi.

Keywords: MIMO antenna; fractal radiating patch; symmetry; WiMAX; WLAN; high isolation; wireless networking; total active reflection coefficient; omnidirectional; multiple input multiple output

1. Introduction

Wideband antennas inherit several attractive features such as a high transfer of data, multiple channel transmission and a low power utility with the ability to capture and transmit a higher resolution of images. Ultrawideband (UWB) was published by the Federal Communication Commission (FCC) of the US in 2002; its bandwidth of 3.10–10.60 GHz leads to applications in many wireless devices such as wearable devices and the Internet of Things. In an uncontrolled environment, a scattering of the signal causes multiple path reflections that reduce the fade effects as well as the bandwidth and efficiency. These problems are encountered by using MIMO technology. The design of a MIMO radiation configuration faces challenges such as achieving a higher isolation between the inter-radiating elements. Two reported research papers [1,2] used fractal flower-shaped geometry where two different substrates were used in the design (FR4 and Rogers RTDuroid5880); both covered the UWB bandwidth for different specific applications when compared with the proposed work. The proposed work was designed for a MIMO configuration for encountering fading of the signals. Discussions of MIMO$_{2\times2}$ antenna configurations are

reported in [3–15] where different techniques were studied resulting in a higher isolation. Placing a pair of L-type slits in the ground increases the isolation below −20 dB [3] and introducing a modified T-type stub and an etched slot on it not only increases the impedance matching but also improves the isolation [4]. Two different dielectric resonator antennas (DRAs) [5,6] were reported that used inserted rectangular DRAs; a single stepped square DR achieved a circular polarization and an effective isolation was achieved using a stub connected to the ground. A port isolation was also achieved when L-shaped slits were added to the ground [7] and a funnel-type stub in the ground [8] was another technique used for isolation purposes. Implementing decoupling strips and a slotted ground also increased the isolation in an EBG structure used to obtain a notched band in an antenna [9]. H-type slots that were etched and connected internally helped in the reduction of cross-polarization and coupling between the placed inter-elements [10]. A unique method of isolation was reported in [11] where a Hilbert fractal and a T-type stub were removed from the ground resulting in a higher isolation [12]. A T-slit embedded in the ground achieved a better isolation in a very wideband dual radiating antenna [13]. A resonator structure between a radiating element [14] and a rectangular strip in the ground are different methods published for the improvement of isolation [13]. Four-element MIMO configurable radiators are discussed in [16–31] where different methods of isolation are used. In [16], orthogonally placed radiators required the absence of any decoupling structure and still maintained a better isolation. The neutralization technique was used for isolation in a $2 \times 2/4 \times 4$ MIMO antenna configuration as reported in [17]; by using a polarization diversity technique, isolation was also improved [16] and a fan-type parasitic decoupler with four strips placed between the radiating elements also provided a higher isolation [19]. A dual notch 4×4 MIMO antenna configuration [18] achieved a better isolation by placing four UWB elements orthogonally to each other. Different decoupling techniques have also been reported such as double-decoupling branches placed orthogonally [21], decoupling elements between two radiators [22] and the orthogonal placement of radiators to further improve isolation [23–29]; circular arc-type grounded stubs also achieved a better isolation [30]. In [31], the absence of a decoupling structure was observed; by placing the four radiating structures orthogonally, a higher isolation was achieved. A flower-type radiating patch antenna has also been reported in [30] that had the capability of mitigating three interfering bands and provided a useful bandwidth of 7.83 GHz. A spanner-shaped dual radiating elements with shared ground and a novel decoupling stub added to ground provides working bandwidth of 7.50 GHz with high isolation [32]. A quasi-self-complimentary MIMO antenna reduced the space and also ensured the bandwidth for UWB applications providing an ECC less than 0.10 [33]. Placing quadra-C strips in between tri-layered vertical slits printed a backplane [34] and a quadruplexing four radiating element antenna was frequency-tunable when a varactor diode was used for covering a frequency band of 4.671–5.841 GHz [35]. Four radiating elements when placed orthogonally and symmetrical [36–41] also provided a better MIMO performance. A tapered microstrip and a semicircular slot in the ground provided a matching of the impedance designed for UWB applications and offered a good diversity performance [40]. The proposed work outclasses the latest literature discussed above where a prototype is developed from an initial design that authenticates the simulated result. Other features of this proposed work are that it offers a high rejection of the interfering bands and is useful for multiband applications.

In this research, four fractal radiating patches are placed orthogonally to each other and the designed MIMO antenna, which provides a wider impedance bandwidth, is useful for UWB/X/partial Ku band applications. Care has also been taken in the mitigation of band-stop filters including WiMAX/WLAN bands. The diversity characteristics of the designed radiator is studied for both $2 \times 2/4 \times 4$ configurations and suggests that the proposed work is capable of higher data rate transmission applications.

In this this work, a novel MIMO antenna in the form of a four-port is also analyzed. It offers a wide impedance bandwidth and a good diversity performance. The proposed

antenna does not have a decoupling structure in the ground or on the plane containing a radiating patch. An analysis of the design methodology and the characterization of $1 \times 1/2 \times 2/4 \times 4$ are discussed in the upcoming sections.

2. Conceptual Design and Hardware Implementation

Figure 1 represents the aspects covering all the optimized dimensions in the implementation of a fractal antenna (FA). As observed from Figure 1a, the antenna had a compact dimension of $W_s \times L_s$ mm^2 where a Rogers RTDuroid5880 microwave substrate of thickness h_s mm was used with electrical properties including $\varepsilon_{permitt.}$ = 2.2 and $\tan \delta_{(loss\ tangent)}$ = 0.0009. A fractal radiation patch was available on the front plane of the microwave substrate used in the current design and on the opposite side to a rectangular ground plane. The signal was fed to the antenna via a microstrip feed line that offered 50 Ω of impedance and a sub-miniature A connector was used with a feed line for the supply of the signal from an external source, which characterized the antenna in the S-parameter and far-field area. The side view is shown by Figure 1b with the thickness of the copper taken as 0.035 mm. Figure 1c signifies the design of a fractal radiator with the front view showing a radiating patch with no notched filters. The radius of the circular radiating was calculated by using Equations (1)–(3) given below, as adapted from [41].

$$M = \frac{K}{\sqrt{\left(1 + \frac{2h_s}{K\pi\varepsilon_r}\left[\ln\left\{\frac{\pi K}{2h_s}\right\} + 1.7726\right]\right)}} \tag{1}$$

$$K = \frac{8.791 \times 10^9}{f_r\ \sqrt{\varepsilon_r}} \tag{2}$$

$$Me = M\sqrt{1 + \frac{2hs}{\pi\varepsilon_r M}\left[\ln\left(\frac{\pi M}{2hs}\right) + 1.7726\right]} \tag{3}$$

where h_s is the height of the substrate, K is a variable parameter dependent on f_r and h_s, f_r = the operating frequency in GHz, M_e = the effective radius in mm, M = the radius of the patch in mm and ε_r = the dielectric permittivity of the substrate.

This provided a working measured bandwidth of 3.75–11.72 GHz and was named Antenna A, as shown by the prototype in Figure 2c. The inscribe of the semicircles, which were twenty in number, was placed on the circumference of the circle with the radius **M** (Figures 1b and 2b). This modification helped to achieve a wider measured bandwidth of 4.07–16.34 GHz. The fractal geometry of Antenna B was converted to an extended bandwidth, which is useful in higher band applications. The proposed antenna contained a partial ground with the dimension $A_1 \times A_3$ mm^2. Figure 1c shows the insertion of the band-stop filters catering for the notched bands of the interfering bands. An inverted T-shaped stub provided the blocking of the WiMAX band whereas a C-type etched slot on the radiator resulted in eliminating the WLAN-interfering bands. All the optimizations of the parameters mentioned in Figure 1 were carried out by using an Electromagnetic Simulator Ansys HFSSv14 tool and the final physical values are recorded in Table 1.
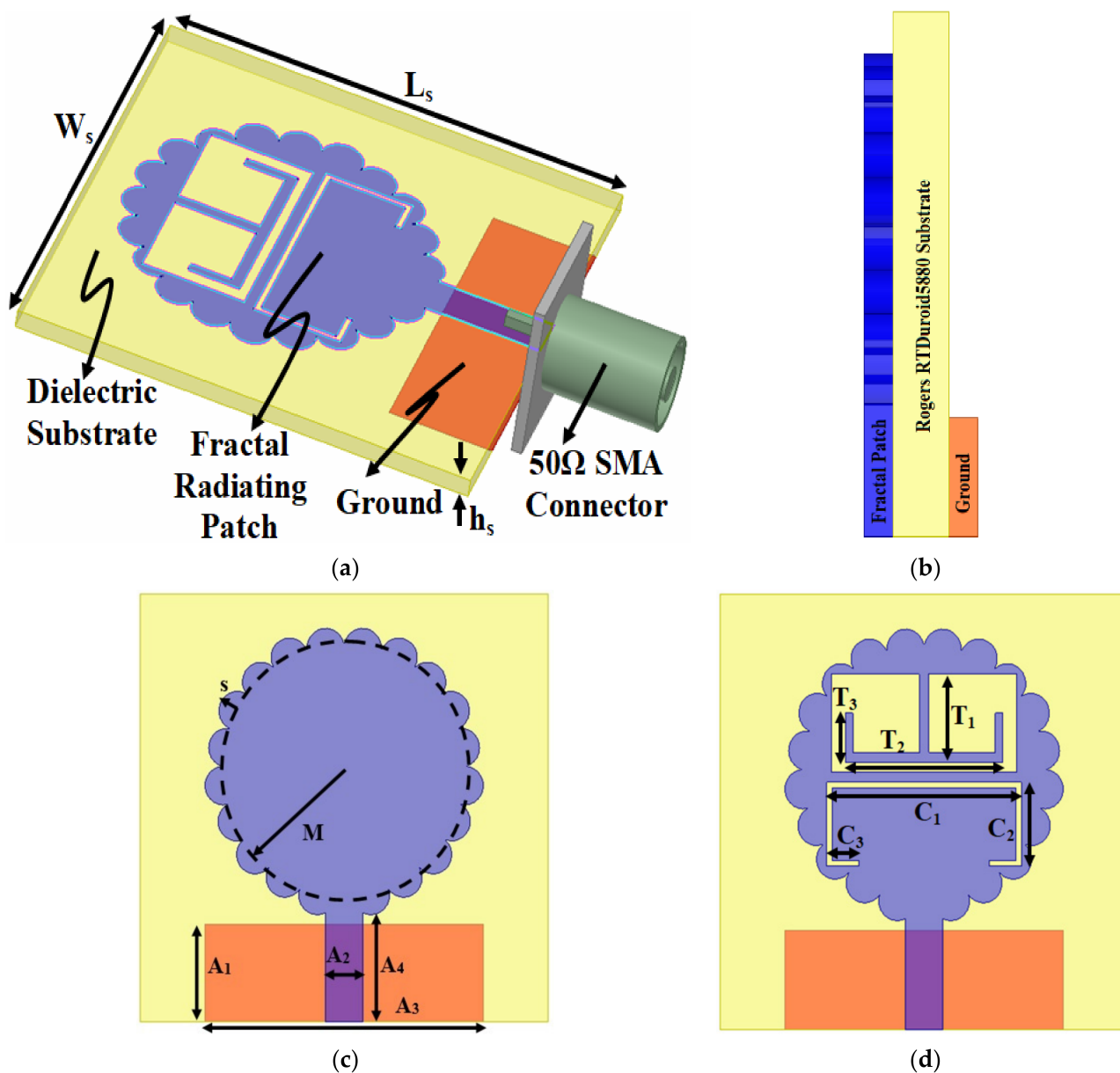
Figure 1. Fractal radiator: (**a**) perspective sight; (**b**) side sight; (**c**) fractal patch and ground (excluding filters); (**d**) fractal patch and ground (including filters).

Table 1. Physical values after optimization.

Par.	mm	Par.	mm	Par.	mm
W_s	22.0	A_2	2.00	T_2	8.50
L_s	22.0	A_4	5.60	T_3	2.50
h_s	0.787	A_3	15.0	C_1	10.50
M	6.50	A_1	5.00	C_2	4.25
s	1.00	T_1	4.50	C_3	1.75
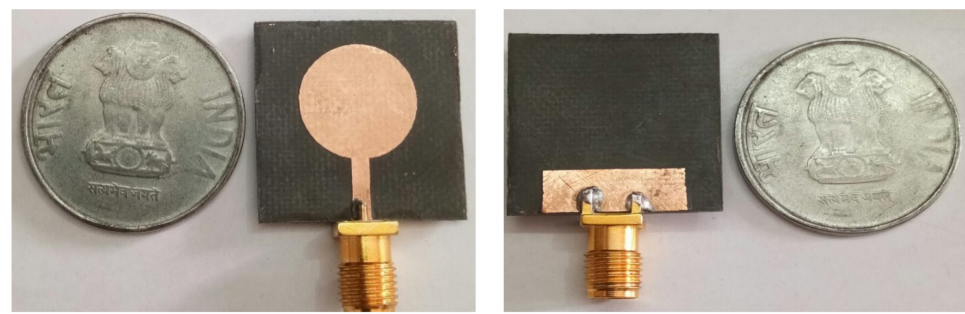
(**a**)

(**b**)
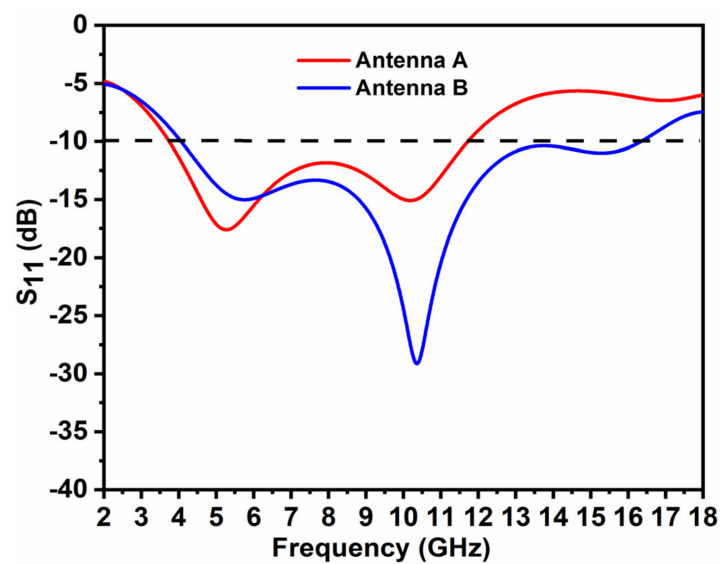
(c)

Figure 2. Development of a solo unit cell without interfering bands: (**a**) prototype of Antenna A; (**b**) prototype of Antenna B; (**c**) measured S-parameters.

3. Analysis of the Key Parameters (Parametric Variation: Notched Bands), Impedance Analysis, Circulation of the Surface Current on the Patch and on the Ground and Time Response Result

A parametric analysis of the key parameters played an important role in not only optimizing the intended design but also achieving a useful bandwidth. In this parametric study, a variation of the length of the ground (A_1 in mm), the radius (M in mm) of the patch circle and the effective length of the notched bands were changed to observe the impact on the operational bandwidth and the change in the position of the centered notched band frequencies. Figure 3a shows the changes in the impedance bandwidth when the length of the ground plane was varied. As per the observation, A_1 varied from 4.00 to 6.00 mm and there was an improvement in the matching of the impedance; for A_1 = 5.00 mm, the intended impedance bandwidth of 4.05–13.93 GHz was achieved. Similarly, when the patch circle radius (designated as M) observed a variation between 6.00 and 7.00 mm, there was a change in the upper cut-off frequency. The value of M = 6.50 mm achieved a desirable operating frequency band of 3.56–12.17 GHz with the best matched impedance.
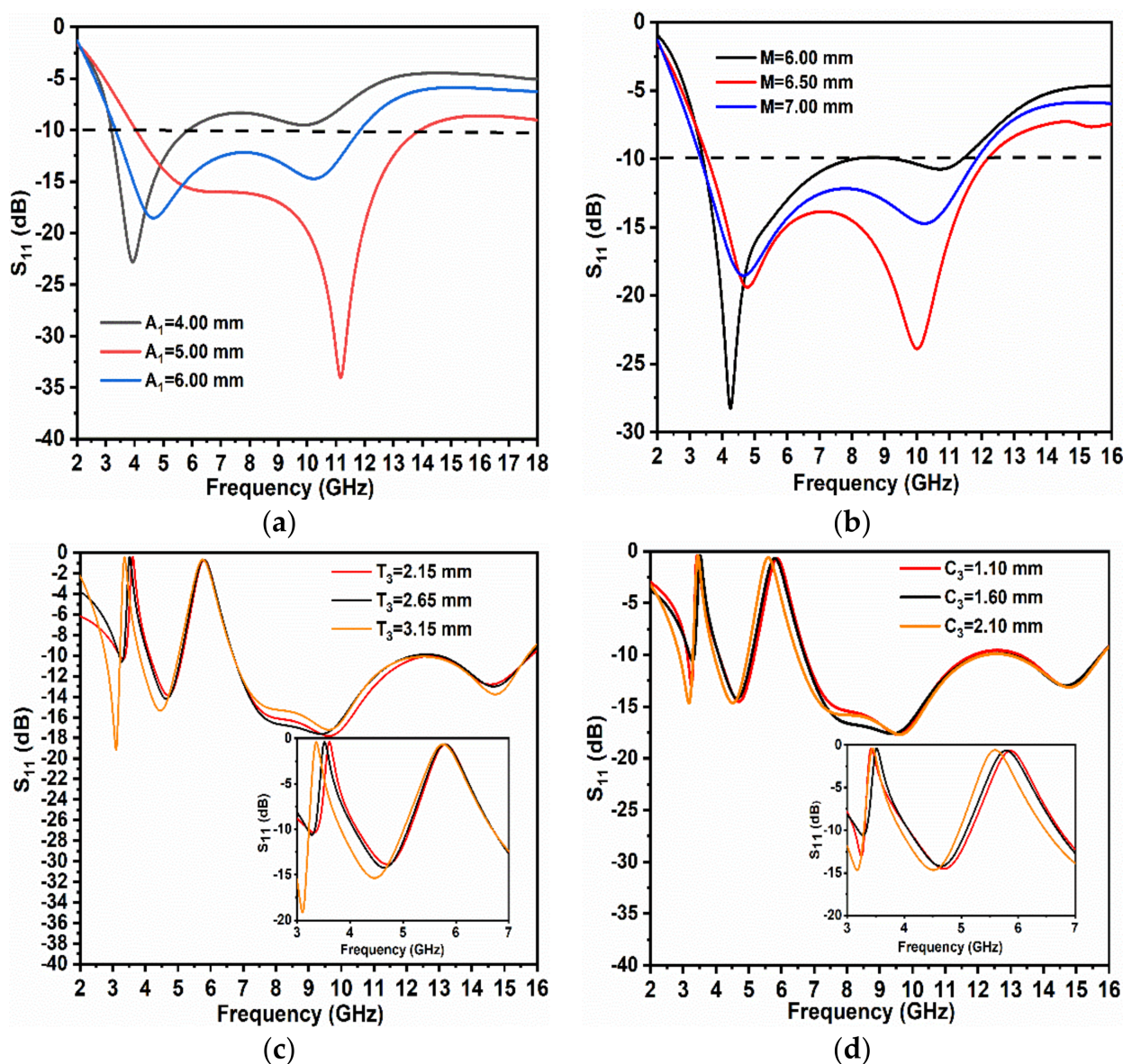
Figure 3. Parameter variation study of (**a**) W_g (ground physical length); (**b**) R (radius of the patch circle); (**c**) T_3 (WiMAX); (**d**) C_3 (WLAN).

Figure 3c,d demonstrates the variations in the physical lengths of the notched filters and the equations affecting these notched filters are given as bellow, as adapted from [5,41].

$$L_{\text{Notch Band}} = c / (2 \times f_{cn} \sqrt{\varepsilon_{reff}}) \tag{4}$$

$$\varepsilon_{reff} = \frac{\varepsilon_r + 1}{2} + \frac{\varepsilon_r - 1}{2} [1 + 12 \frac{h_s}{A_2}]^{\frac{-1}{2}}. \tag{5}$$

Here, f_{cn} is the center notched frequency in GHz of the interfering bands, Wm is the width of the microstrip in mm and *hs* is the height of substrate in mm.

For the WiMAX notched band, a variation of T_3 from 2.15 to 3.15 mm was observed in the change of bandwidth from 3.38–4.14 GHz (maximum RL = −0.37 dB at 3.61 GHz) to 3.22–3.83 GHz (maximum RL = −0.43 dB at 3.36 GHz). The fixed dimension of T_3 = 2.65 mm; the intended WiMAX notch band of a bandwidth 3.33–4.09 GHz was achieved with a maximum RL of −0.39 dB at 3.52 GHz. The total dimension of the T-type stub was $L_{\text{WiMAX}} = T_1 + T_2 + 2T_3$ mm. Similarly, for the WLAN notched band, a variation of C_3 from 1.10 to 2.10 mm recorded a shifting from 5.17–6.74 GHz (maximum RL = −0.685 dB at 5.87 GHz) to 4.97–6.49 GHz (maximum RL = −0.61 dB at 5.60 GHz). For the optimized value of C_3 = 1.60 mm, the required notched band of 5.09–6.70 GHz with a maximum RL of −0.68 dB at 5.77 GHz was achieved. The total length of the slot was calculated as $L_{\text{WLAN}} = C_1 + 2C_2 + 2C_3$ mm. The optimization of the notched bands ensured that the three working bands were preserved.

Figure 4a,b shows the impedance graphs for a single unit cell antenna with the exclusion/inclusion of the notched bands. As per the observation, for the antenna without notched bands, the real and imaginary impedance should ideally be 50 Ω and 0 Ω, respectively, but for the proposed antenna, the real and imaginary impedance almost followed the said values. Figure 4b shows the discrepancy of the impedance; for the WiMAX band, the real and imaginary values corresponded with 92.23–94j Ω, which was a very high mismatch condition. Similarly, for the WLAN notched band, the values were 2–12j Ω, which was again a mismatch situation. This mismatch condition for both notched bands ensured the reflection of the input signal and, hence, the filter characteristics were achieved.

The surface distribution of the current for the interfering bands is depicted in Figure 4c,d. For 3.45 GHz, the maximum distribution of the current density on the surface was observed inside a rotated T-type stub. At 5.70 GHz, the maximum distribution of the current density on the surface was also observed around the C-type slot used to notch the WLAN band. This led to the conclusion that all the input signals for both notched bands observed a deterioration of impedance and, hence, this resulted in the band rejection characteristics.

The degree of distortion of the pulse was evaluated by studying the group delay. Figure 5a shows the group delay of the proposed antenna, which signified that the variations were less than 0.2 ns for the bandwidth of 3–9 GHz and fewer than 0.5 ns for the remaining operating bands. The impulse response given as the input for the transmitter in both alignments (face-to-face and side-to-side) is depicted in Figure 5b. A Gaussian pulse was applied at the transmitting antenna. It was observed that in the face-to-face orientation, larger amplitude signals were received compared with the side-to-side alignment as expected.
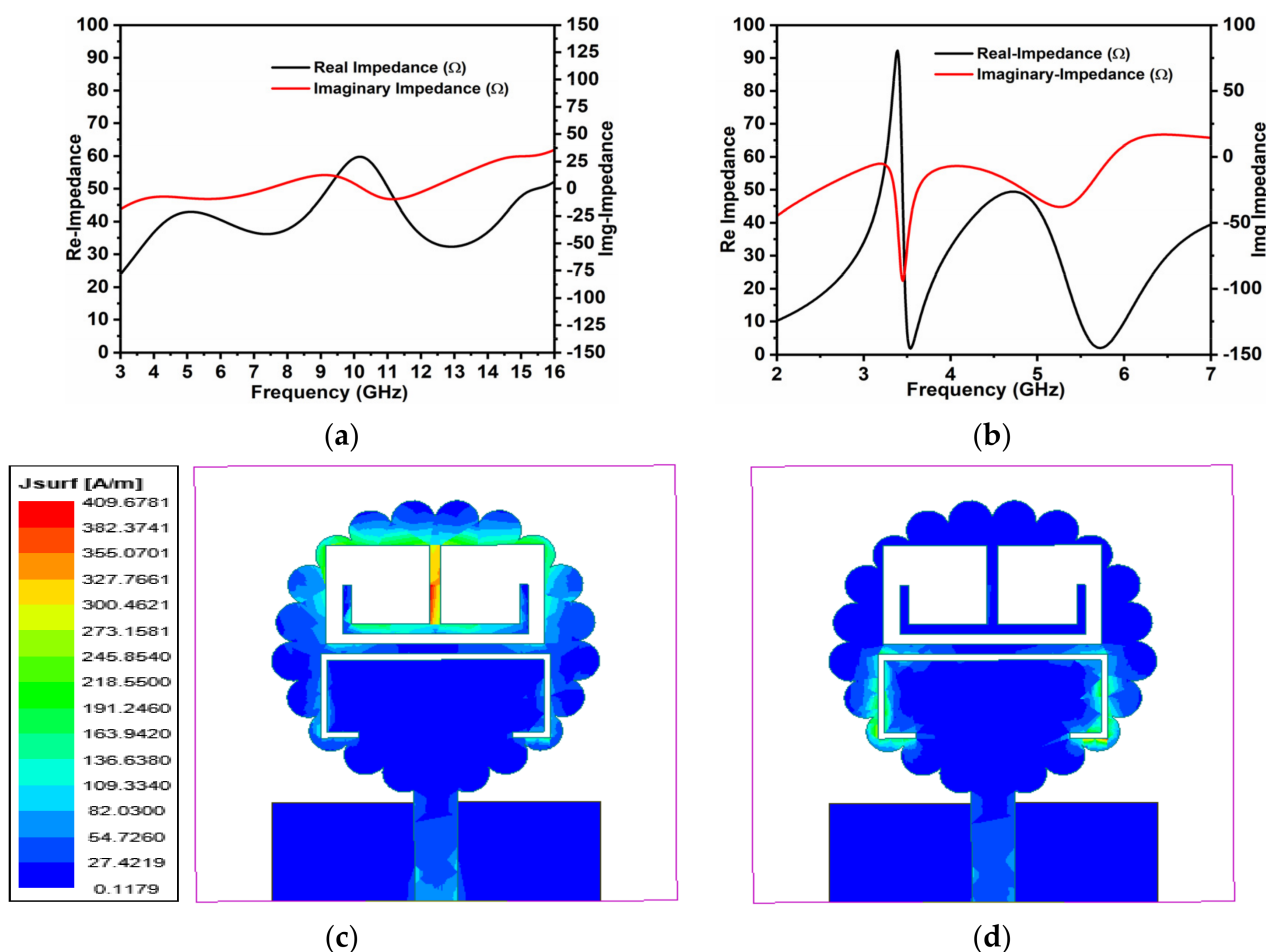
Figure 4. (**a**) Real and imaginary impedance (exclusion of filters); (**b**) real and imaginary impedance (inclusion of filters); (**c**) the impedance of the antenna with filtering bands; (**d**) the distribution of the current density on the surface at 3.45 and 5.70 GHz, correspondingly.
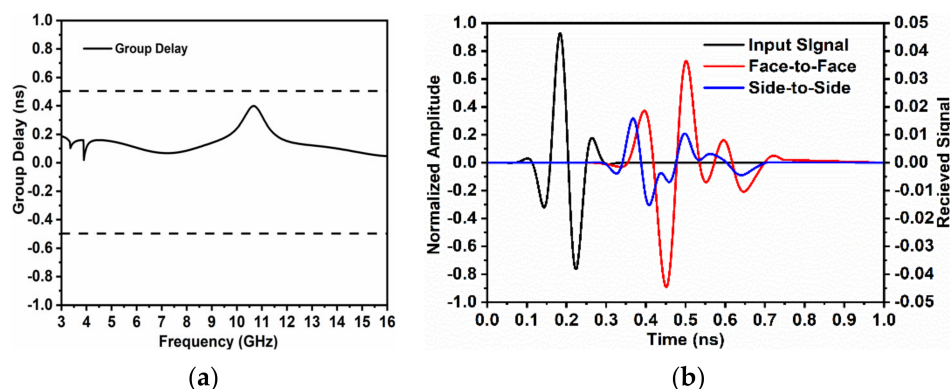
Figure 5. Time response of a single unit cell: (**a**) group delay; (**b**) impulse response.

4. Characterization of the 2 × 2 MIMO Antenna

In Section 3, a single unit cell characterization was designed and analyzed and the solo antenna was transformed to a two-port MIMO configuration to increase the efficiency and also to encounter multiple fading effects. Figure 6a shows the proposed fabricated two-port MIMO arrangement, which was a result of placing two identical radiators in an orthogonal manner with a spacing of λ/2 between them. As per the observation, there was an absence of an additional decoupling element with a better separation of the transmission coefficients. The antenna dimension of the new MIMO configuration was

$L_s \times 2W_s$ mm^2. Figure 6b shows a plot of the S-parameters for both the reflection and transmission coefficients. The S-parameters play a vital role in achieving the characteristics of the MIMO antenna as all these above parameters are useful in the calculation of the diversity characteristics for the designed radiator. The bandwidth was also calculated from the obtained S-parameters. For both the radiating patches, the S_{11}/S_{22} parameters achieved the intended -10 dB operational bandwidth and filtered the WiMAX and WLAN frequency bands. As per the depiction in Figure 6b, the antenna offered a better isolation of -20 dB in the bandwidth of interest providing an acceptable diversity performance.
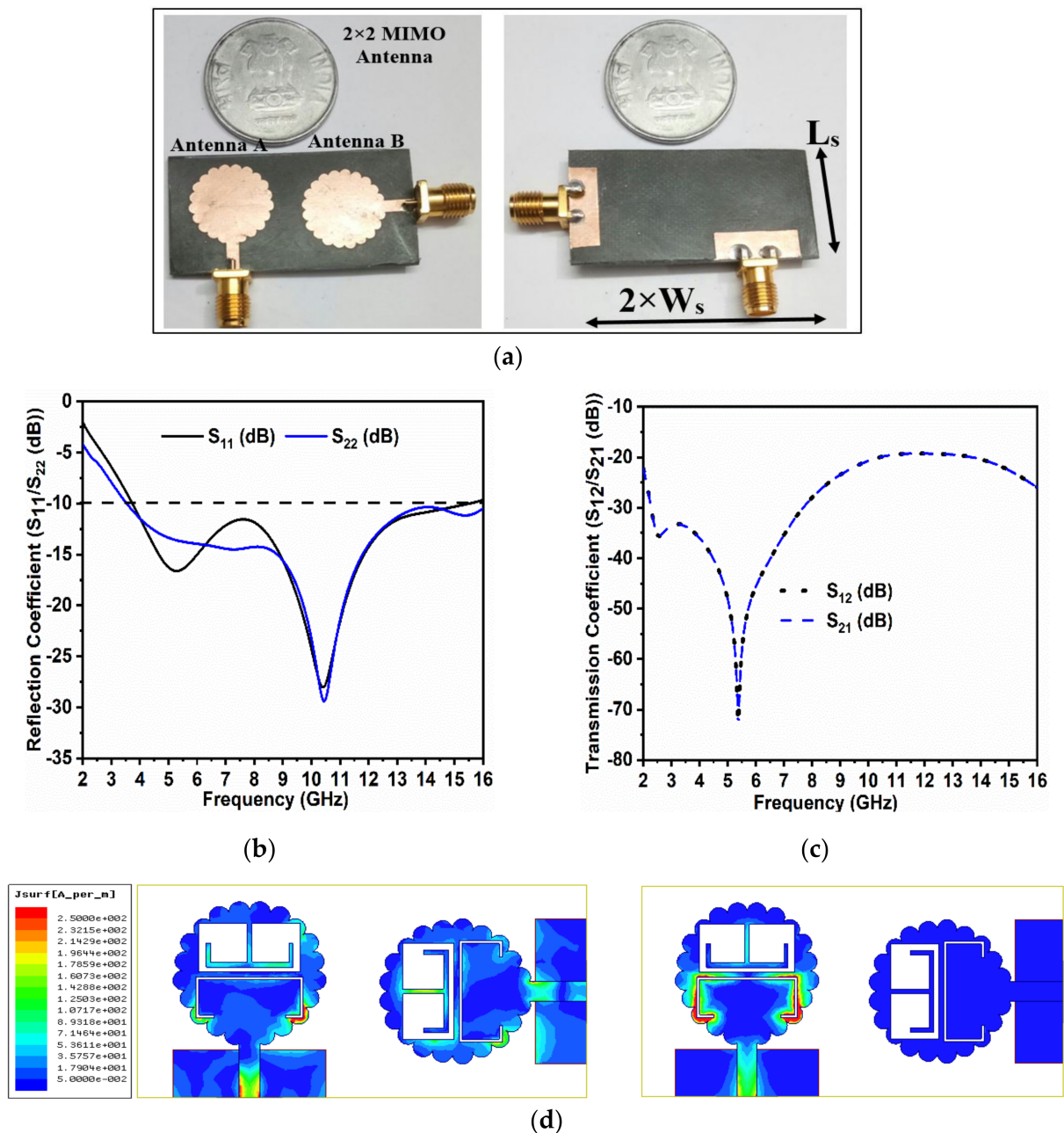
Figure 6. Two-port antenna: (**a**) prototype (front and ground); (**b**) reflection coefficients (S_{11}/S_{22}); (**c**) transmission coefficients (S_{12}/S_{21}); (**d**) distribution of the current density on the surface at 3.54 and 5.53 GHz, respectively.

Figure 6c,d observes the distribution of the current density on the surface, which was simulated for 3.54 and 5.53 GHz, respectively. This simulation was carried out by matching

the port of Antenna B and providing an input to Antenna A. As per the observations, a conclusion was derived that the distribution of the current density on the surface was observed inside the T-type inverted stub and the outer boundary of the C-type slot. This again led to the conclusion that a highly mismatched impedance occurred and, hence, the input signals were reflected leading to the notched band characteristics as observed from the S_{11}/S_{22} graph.

The verification of the prototype is shown in Figure 6a on behalf of the diversity characteristics of the antenna studied where ECC $_{2\times2}$, DG $_{2\times2}$, TARC $_{2\times2}$ and CCL $_{2\times2}$ are discussed. These results were obtained based on the S-parameter graph.

The envelope correlation coefficient was calculated utilizing the radiating field patterns and based on the S-parameters. For the radiating field pattern, ECC was given by [3] as follows.

$$\rho_e = \frac{\left| \iint\limits_{4\pi} \left[\vec{F_1}(\theta,\phi) \times \vec{F_2^*}(\theta,\phi) \right] d\Omega \right|^2}{\iint\limits_{4\pi} \left| \vec{F_1}(\theta,\phi) \right|^2 d\Omega \left| \vec{F_2}(\theta,\phi) \right|^2 d\Omega}$$

(6)

where ρ_e is ECC for the two different fields, $\vec{F_1}(\theta,\phi)$, $\vec{F_2^*}(\theta,\phi)$ are the field patterns (electric field intensity: V/m) of the two different radiating elements and $d\Omega$ is the unit solid angle. Equation (6) signifies that the radiation pattern of the ith port was calculated by matching all the leftover ports to 50 Ω, which is shown as $\vec{F_i}(\theta,\phi)$. For any MIMO system with S number of radiating elements considering any two antenna systems, m and n are obtained by:

$$\rho_e(m,n,S) = \frac{|C_{m,n}(S)|^2}{\prod\limits_{K=m,n} [1 - C_{k,k}(S)]}$$

(7)

where $C_{m,n}(S)$ is given by:

$$C_{m,n}(S) = \sum_{s=1}^{S} S_{m,s}^* S_{s,n}$$

(8)

where $C_{m,n}$ is the discrete function of the S-parameters and $S^*_{m,s}$ and $S_{s,n}$ are the complex and real parts of the S-parameters.

From Equations (7) and (8):

$$\rho_e(m,n,S) = \frac{\left| \sum\limits_{s=1}^{S} S_{m,s}^* S_{s,n} \right|^2}{\prod\limits_{s=m,n} \left[1 - \sum\limits_{s=1}^{S} S_{m,s}^* S_{s,n} \right]}.$$

(9)

For a 2 × 2 MIMO configuration antenna from the S-parameter, the ECC is given by:

$$\text{ECC} = \frac{\left| S_{11}^* S_{12} + S_{21}^* S_{22} \right|^2}{\left((1 - |S_{11}|^2 - |S_{21}|^2) \left(1 - |S_{22}|^2 - |S_{12}|^2 \right) \right)}.$$

(10)

Equation (10) calculates the ECC from the S-parameter. It is well known that for any uncorrelated MIMO scheme, the ECC is always ideally zero. In a non-ideal case, the value of ECC $_{2\times2}$ must be below 0.40; for the reported MIMO antenna configuration, the values were 0.03, as observed in Figure 7a. Another diversity performance called the directive gain was calculated from the equation shown below [7]:

$$\text{DG}_{2\times2} = 10\sqrt{1 - ECC_{2\times2}^2}.$$

(11)
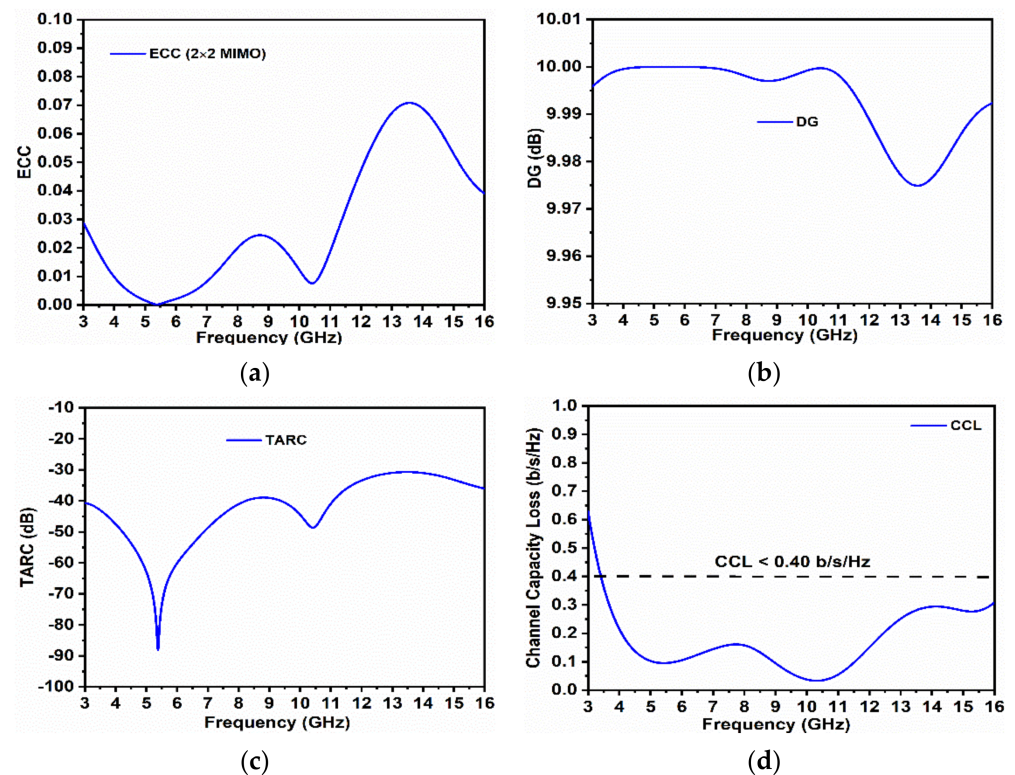
Figure 7. Diversity 2 × 2 results: (**a**) ECC; (**b**) DG; (**c**) TARC; (**d**) CCL.

For the MIMO radiating system, the DG $_{2 \times 2}$ values should be more than 9.95 dB. As per the observation in Figure 7b, in the entire operating bandwidth of interest, the recorded values were DG $_{2 \times 2}$ > 9.97 dB.

The MIMO configuration faces challenges such as design challenges to obtain a high isolation between the radiating elements. A result analysis based on S_{11}/S_{22} and S_{12}/S_{21} alone could not characterize the MIMO configuration and, hence, a new calculating parameter, namely, TARC $_{2 \times 2}$ was calculated, which is given by Equation (12) below [7]:

$$\text{TARC} = \sqrt{\frac{(S_{11} + S_{12})^2 + (S_{21} + S_{22})^2}{2}}. \tag{12}$$

Here S_{11}, S_{12}, S_{21} and S_{22} are the S-parameters in dB. For ideal conditions, TARC $_{2 \times 2}$ < 0.0 dB and for the projected diversity antenna, these values were > −20.0 dB in the whole application band.

The capacity of the MIMO channel was another diversity performance parameter that signified the faithful transmission of information without any distortion. The CCL for the 2 × 2 MIMO was given by [16]:

$$CCL = -\log_2(\psi^R). \tag{13}$$

Here (ψ^R) is the 2 × 2 matrix for the 2 × 2 MIMO and ψ_{11}, ψ_{12}, ψ_{21} and ψ_{22} are the matrix coefficients.

$$\psi^R = \begin{bmatrix} \psi_{11} & \psi_{12} \\ \psi_{21} & \psi_{22} \end{bmatrix} \tag{14}$$

$$\psi_{11} = 1 - \left[|S_{11}|^2 + |S_{12}|^2 \right] \tag{15}$$

$$\psi_{22} = 1 - \left[|S_{22}|^2 + |S_{21}|^2 \right] \tag{16}$$

$$\psi_{12} = -[S_{11}{}^* S_{12} + S_{21}{}^* S_{12}] \tag{17}$$

$$\psi_{21} = -[S_{22}{}^* S_{21} + S_{12}{}^* S_{21}]. \tag{18}$$

Figure 7d shows that the CCL for the projected diversity antenna configuration was well below 0.40 bits/s/Hz, which was a permissible value.

5. Characterization of the 4 × 4 MIMO Antenna

In the previous section, the characterization of the 2 × 2 MIMO configuration was discussed. To achieve a higher data rate of transmission, the proposed 2 × 2 MIMO was transformed to a MIMO (4 × 4) arrangement by the addition of two more identical radiating patches that were located orthogonally with respect to each other, as observed in Figure 8a. The proposed MIMO antenna occupied a compact space with antenna dimensions of $2L_s \times 2W_s$ mm^2, designed on a Rogers RTDuroid5880 substrate (Figure 8b,c). Figure 8d,e shows the surface density of the current circulation at 3.52 and 5.58 GHz. It was noted and observed that the circulation of the current density on the surface accumulated inside the inverted T-alphabet structure for the WiMAX filter and around the C-alphabet etched structure in the case of the WLAN filter. This indicated that these two notched bands offered a higher change in the impedance and, hence, resulted in the non-radiation of the input signals. Figure 8f depicts the scattering parameters for the notched filter-designed antenna. It was observed that the required bandwidth with the notched bands was achieved by noting the $S_{11}/S_{22}/S_{33}/S_{44}$ S-parameters. Figure 8g shows the measured S-parameters (reflection coefficients), which had a good agreement with the simulated results. The Anritsu VNA (model number MS2038C) was used for the S-parameter measurement and an anechoic chamber with a capacity of 20 GHz was used for the far-field measurements.

The diversity results included the ECC and DG. The ECC for the 4×4 MIMO configuration was given by Equation (19) [20]:

$$\text{ECC}_{\text{MIMO4}\times 4} = \frac{\left| S_{11}^* \, S_{12} \, + \, S_{21}^* \, S_{22} + S_{13}^* \, S_{32} \, + \, S_{14}^* \, S_{42} \right|^2}{\left(\left(1 - |S_{11}|^2 - |S_{21}|^2 - |S_{31}|^2 - |S_{41}|^2 \right) \left(1 - |S_{12}|^2 - |S_{22}|^2 - |S_{32}|^2 - |S_{42}|^2 \right) \right)}. \tag{19}$$

As it is known, ECC < 0.5 lies below for any diversity antenna. For the current reported antenna, the simulated values were < 0.05 and for the measured results these values were <0.1. In both cases, the ECC values rose in the notched bands (WiMAX and WLAN) due to the non-operating condition of the proposed antenna. Similarly, the directive gain of the reported work for multiband applications was obtained by Equation (20) [7]:

$$\text{DG} = \sqrt{1 - \rho^2_{e(1,2,4)}}. \tag{20}$$

The above equation calculates the DG for a 4 × 4 MIMO antenna configuration. For any MIMO configuration, DG > 9.95 dB; in the reported work, both the simulation and measuring values corresponded well above 9.95 dB except in the notched bands, as observed in Figure 9c,d.

(a)   (b)   (c)

Figure 8. *Cont.*

(**d**)   (**e**)

(**f**)   (**g**)
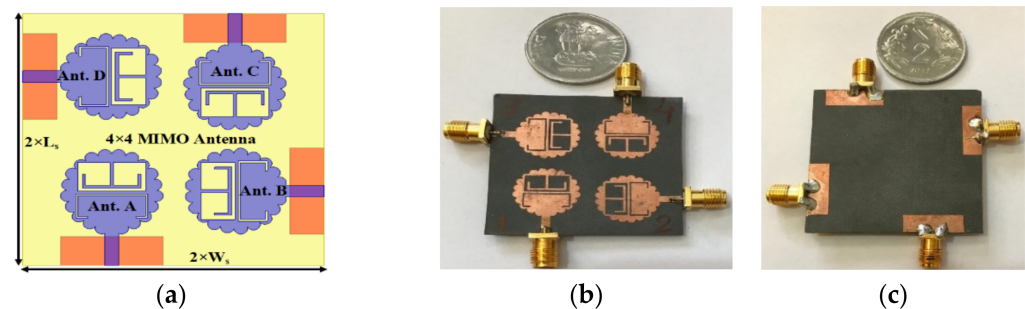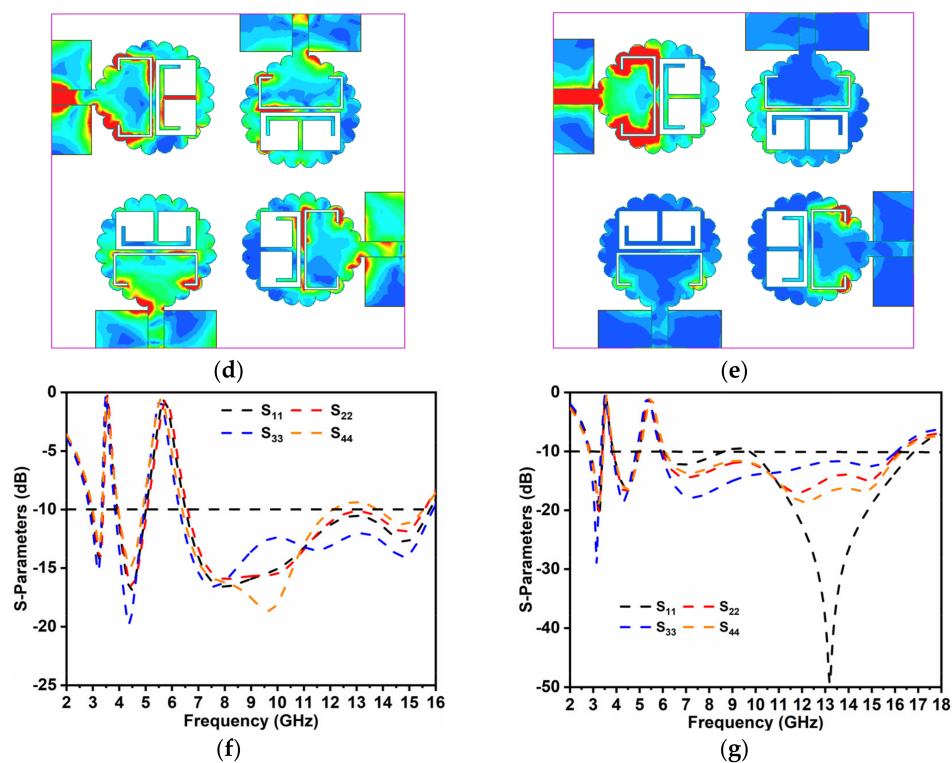
Figure 8. Diversity results: (**a**) simulator snapshot; (**b**,**c**) hardware photographs (radiating and round view); (**d**) SCFD at 3.52 GHz; (**e**) SCFD at 5.58 GHz; (**f**,**g**) simulated and measured.

(**a**)   (**b**)

(**c**)   (**d**)
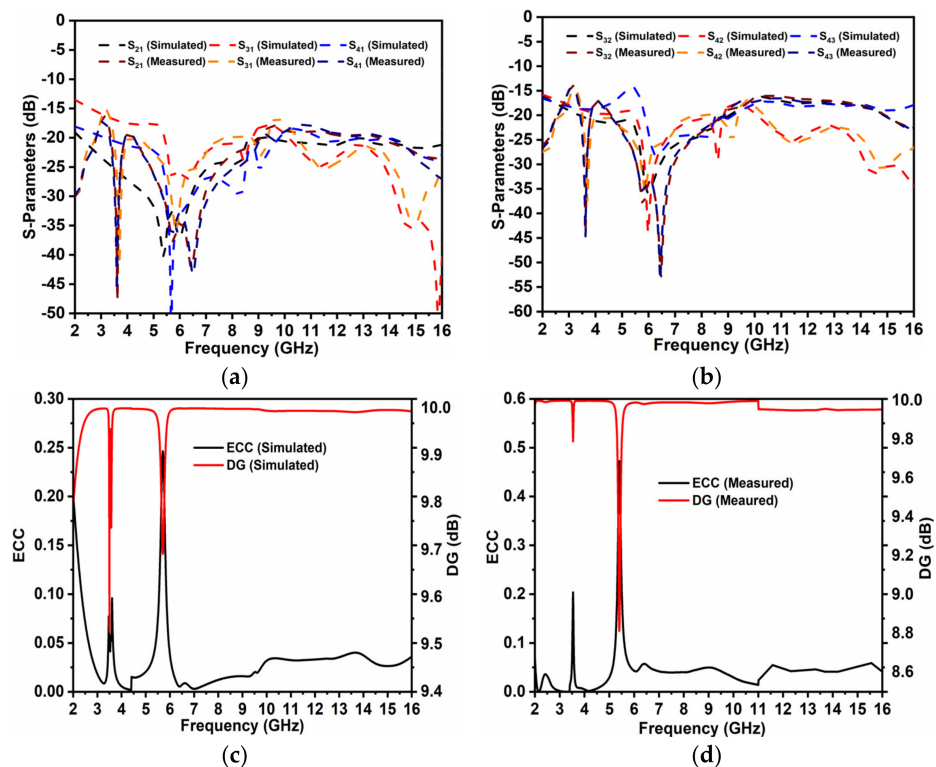
Figure 9. S-parameters (transmission coefficients): (**a**) $S_{21}/S_{31}/S_{41}$ simulated and measured; (**b**) $S_{32}/S_{42}/S_{43}$ simulated and measured; (**c**) simulated ECC and DG; (**d**) measured ECC and DG.

6. Discussion of the Results (MIMO$_{4 \times 4}$ Antenna)

Figure 10 depicts the comparison of the simulation/measured results of the reported work. Table 2 offers a comparative analysis of the simulated/measured VSWR comparison, which is tabulated in Figure 10a. It was concluded that the simulated result almost matched with the measured results. The permissible deviation in the comparison may be due to the fabrication process and the SMA soldering. Figure 10b shows the plot of the far-field result in terms of the measured gain and radiation efficiency. As per the observation, the reported MIMO antenna maintained an average realized gain of 4.07 dBi in the application bandwidth. There was a sharp fall of gain in the filtered bands, as noted in Figure 10b. This steep fall in gain corresponded with −12.78 at 3.59 GHz and −14.96 at 5.58 GHz, respectively. This was due to the antenna not radiating in the notched bands. Similarly, the proposed antenna offered a maximum radiation efficiency of 89% and there was also a decrease in efficiency to 28% at 3.69 GHz and 23% at 5.59 GHz, respectively. Figure 10c shows the VNA measurement setup of the proposed 4 × 4 MIMO antenna configuration where one of the ports was connected to one of the ports of the VNA; the reflection coefficients (Saa: $S_{11}/S_{22}/S_{33}/S_{44}$ where a = 1,2,3,4) were measured and the remaining ports were matched to their characteristic impedance (50 Ω). Figure 10d shows the anechoic chamber setup for the measurement of gain and the 2-D radiating pattern of the reported work. The gain measurement was carried out by using two identical antennas and was calculated by the Friis transmission formula [42]:

$$P_R = \frac{P_T \, G_T \, G_R \, \lambda^2}{(4\pi R)^2}. \tag{21}$$
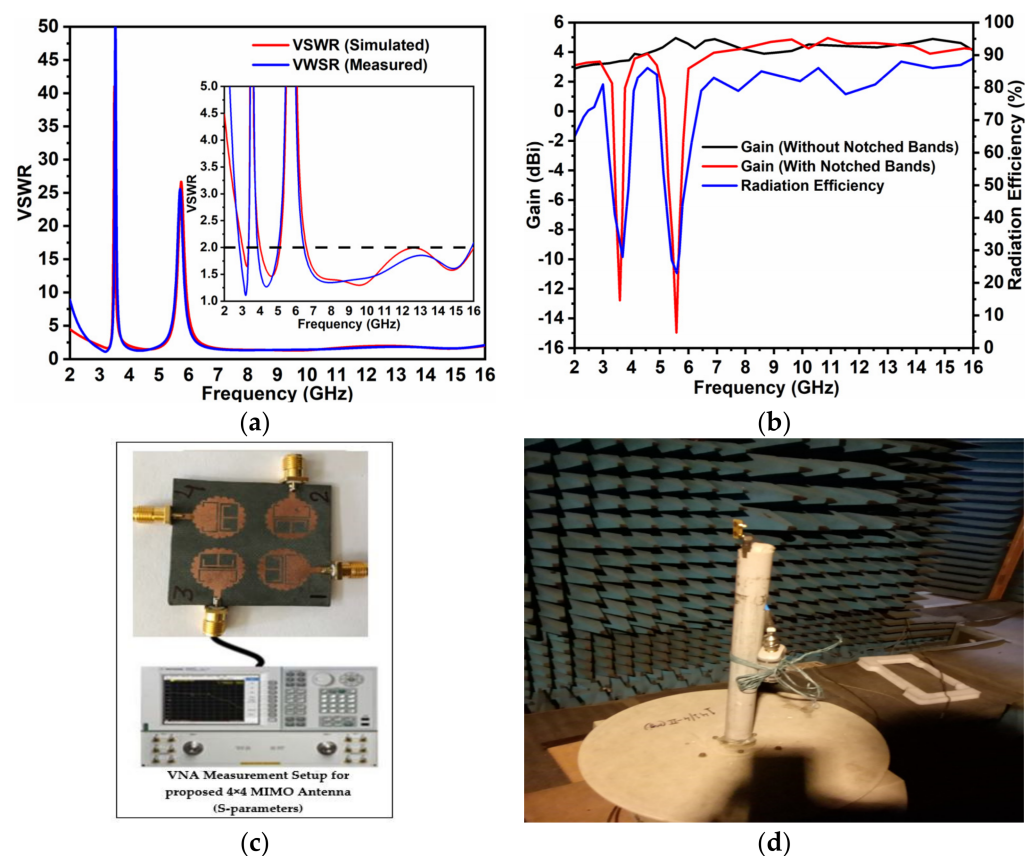
Figure 10. Simulation/measured results comparison: (**a**) VSWR (simulated and measured); (**b**) measured gain and radiation efficiency; (**c**) VNA measurement setup of the S-parameters; (**d**) gain and radiation pattern measurement setup inside the anechoic chamber.

Table 2. Simulated and measured VSWR comparison.

	WiMAX (GHz)	WLAN (GHz)	Bandwidth (GHz)
Simulated	3.31–3.98	5.12–6.59	3.02–15.98
Measured	3.36–3.86	5.03–6.46	2.84–15.88

As both antennas were identical, $G_T = G_R = G_P$ (dB):

$$G_P = \frac{4\pi R \sqrt{P_R}}{\lambda \sqrt{P_T}}. \tag{22}$$

Here, P_R is the power received by the receiver (watts), P_T is the power transmitted by the transmitter (watts), G_T is the gain of the transmitter (dB), G_R is the gain of the receiver (dB), λ is the wavelength (m) and R is the distance between the transmitter and the receiver considering the far-field region.

Figure 11 shows the measured radiation pattern of the reported work in the principal E- and H-planes. As per the observation, the antenna offered a di-pole-like pattern and an omnidirectional pattern, which were required for the operation of the proposed antenna. These radiating patterns were observed and measured at 4.50, 6.85 and 11.0 GHz.
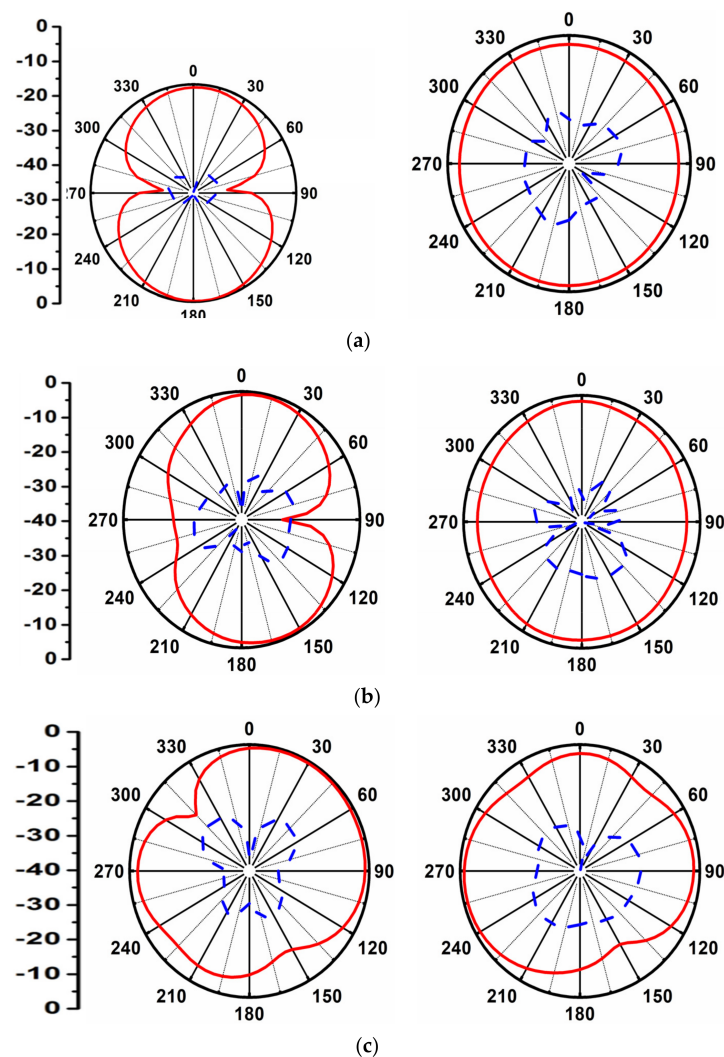
Figure 11. The 2-D radiation pattern of the reported work at (**a**) 4.50 GHz; (**b**) 6.85 GHz; (**c**) 11.0 GHz.

7. Evaluation of the Reported Work with Present State-Of-The-Art Technology

Table 3 shows a comparison of the reported work with earlier reported works. It could be concluded that the proposed MIMO antenna configuration had several advantages over the other designs in the aspect of a wide useable impedance bandwidth that can be used for various applications in the wireless field. The proposed antenna utilized a Rogers RTDuroid5880 substrate, which gave excellent results both in terms of the S-parameter and the far-field results. In comparison with the other published works, the proposed antenna offered a very high rejection of the interfering bands, which was not achieved in the other published works. Due to the larger bandwidth (2.84–15.88 GHz in the MIMO$_{4\times4}$), the proposed antenna may have applications in UWB including for various imaging techniques such as through-wall imaging, medical applications, surveillance systems, ground-penetrating radar systems, satellite applications and RADAR applications in X and partial Ku bands. Compared with the other designs with dual notched band characteristics, the proposed antenna was also compact.

Table 3. Evaluation of the reported work compared with other published works.

Ref.	No. of Ports	Antenna Size (mm³)	Bandwidth (GHz)	No. of Notched Bands	Notched Bands	ECC	DG (dB)	CCL (bits/s/Hz)	Isolation (dB)	Gain (dBi)
[14]	04	80 × 80 × 1.52	3.18–11.5	-	-	<0.015	>9.95	<0.50	<−10	7.48
[15]	04	48 × 34 × 1.60	3.52–10.08	-	-	<0.039	>9.81	<0.29	<−23	2.86
[16]	04	38.3 × 38.3 × 0.8	3.00–13.2	1	WLAN	<0.02	-	-	<−17	4.10
[17]	04	67 × 67 × 1.60	3.50–20.0	1	WLAN	<0.01	-	-	<−20	4.70
[18]	04	50 × 50 × 0.787	2.20–10.4	2	WiMAX WLAN	<0.30	-	-	<−14	6.80
[19]	04	40 × 40 × 1.60	3.00–18.0	1	WiMAX	<0.03	>9.95	-	<−20	4.00
[20]	04	72 × 72 × 0.80	2.80–13.3	2	WiMAX WLAN	<0.06	-	-	<−18	5.08
[23]	04	31 × 31 × 0.762	3.60–10.6	-	-	<0.03	-	-	<−20	5.02
[24]	04	40 × 40 × 1.60	2.60–10.6	2	WiMAX WLAN	<0.07	-	<0.4	<−20	-
[26]	04	40 × 40 × 1.60	3.10–11.0	-	-	<0.005	-	<0.4	<−20	3.28
* P	**02**	**22 × 44 × 0.787**	**2.88–15.76**	**2**	**WiMAX WLAN**	**<0.01**	**>9.95**	**<0.4**	**<−20**	**−3.52**
	04	**44 × 44 × 0.787**	**2.84–15.88**	**2**	**WiMAX WLAN**	**<0.01**			**<−15**	

* *P* (Proposed Antenna).

8. Conclusions

This work presented a UWB extended bandwidth compact monopole 4 × 4 MIMO antenna and all four radiating patches were in symmetry, which provided a better isolation <−15dB in the operating band of interest. Due to the larger bandwidth of 2.84–15.88 GHz, the proposed MIMO antenna may be useful for applications in UWB as well as X and partial Ku bands. The antenna also offered resistance to WiMAX and WLAN-interfering bands by the introduction of notched band filters on the radiating patch. The antenna also offered a peak average gain of 3.52 dBi including a maximum radiating efficiency of 89%. Different several diversity metrics including ECC, DG and TARC were calculated, which were found to be within the permissible limits. Due to the above merits, the proposed MIMO antenna is suitable for portable UWB devices/gadgets, RADAR and satellite applications. The omnidirectional pattern of the MIMO antenna at different frequency bands also ensures a larger area coverage for the above applications.

Author Contributions: Conceptualization, M.S., P.C.V. and N.G.; methodology, D.A., I.A. and A.H.M.; validation, N.G., D.A. and A.H.M.; formal analysis, M.S. and P.C.V.; investigation, I.A.; resources, A.H.M.; data curation, D.A.; writing—original draft, M.S., P.C.V. and N.G.; writing—review and editing, D.A. and I.A.; supervision, A.H.M.; project administration, I.A. and D.A. All authors have read and agreed to the published version of the manuscript.

References

1. Sharma, M.; Awasthi, Y.K.; Singh, H.; Kumar, R.; Kumari, S. Design of Compact Flower Shape Dual Notched-Band Monopole Antenna for Extended UWB Wireless Applications. *Frequenz* **2016**, *70*, 499–506. [CrossRef]
2. Sharma, M.; Awasthi, Y.K.; Singh, H.; Kumar, R.; Kumari, S. Compact UWB Antenna with High Rejection Triple Band-Notch Characteristics for Wireless Applications. *Wirel. Pers. Commun.* **2017**, *97*, 4129–4143. [CrossRef]
3. Haq, M.A.U.; Koziel, S. Ground Plane Alterations for Design of High-Isolation Compact Wideband MIMO Antenna. *IEEE Access* **2018**, *6*, 48978–48983. [CrossRef]
4. Li, W.; Hei, Y.; Grubb, P.M.; Shi, X.; Chen, R.T. Compact Inkjet-Printed Flexible MIMO Antenna for UWB Applications. *IEEE Access* **2018**, *6*, 50290–50298. [CrossRef]
5. Abedian, M.; Rahim, S.K.A.; Fumeaux, C.; Danesh, S.; Lo, Y.C.; Jamaluddin, M.H. Compact ultrawideband MIMO dielectric resonator antennas with WLAN band rejection. *IET Microw. Antennas Propag.* **2017**, *11*, 1524–1529. [CrossRef]
6. Sahu, N.K.; Das, G.; Gangwar, R.K. Dielectric resonator-based wide band circularly polarized MIMO antenna with pattern diversity for WLAN applications. *Microw. Opt. Technol. Lett.* **2018**, *60*, 2855–2862. [CrossRef]
7. Chandel, R.; Gautam, A.K.; Rambabu, K. Tapered Fed Compact UWB MIMO-Diversity Antenna with Dual Band-Notched Characteristics. *IEEE Trans. Antennas Propag.* **2018**, *66*, 1677–1684. [CrossRef]
8. Gautam, A.K.; Yadav, S.; Rambabu, K. Design of Ultra–Compact Uwb Antenna with Band–Notched Characteristics for Mimo Applications. *IET Microw. Antennas Propag.* **2018**, *12*, 1895–1900. [CrossRef]
9. Jaglan, N.; Gupta, S.D.; Thakur, E.; Kumar, D.; Kanaujia, B.K.; Srivastava, S. Triple band notched mushroom and uniplanar EBG structures based UWB MIMO/Diversity antenna with enhanced wide band isolation. *AEU-Int. J. Electron. Commun.* **2018**, *90*, 36–44. [CrossRef]
10. Acharjee, J.; Mandal, K.; Mandal, S.K. Reduction of mutual coupling and cross-polarization of a MIMO/diversity antenna using a string of H-shaped DGS. *AEU-Int. J. Electron. Commun.* **2018**, *97*, 110–119. [CrossRef]
11. Gorai, A.; Dasgupta, A.; Ghatak, R. A compact quasi-self-complementary dual band notched UWB MIMO antenna with enhanced isolation using Hilbert fractal slot. *AEU-Int. J. Electron. Commun.* **2018**, *94*, 36–41. [CrossRef]
12. Chandel, R.; Gautam, A. Compact MIMO/diversity slot antenna for UWB applications with band–notched characteristic. *Electron. Lett.* **2016**, *52*, 336–338. [CrossRef]
13. Sharma, M. Design and Analysis of MIMO Antenna with High Isolation and Dual Notched Band Characteristics for Wireless Applications. *Wirel. Pers. Commun.* **2020**, *112*, 1587–1599. [CrossRef]
14. Ghosh, C.K.; Pratap, M.; Kumar, R.; Pratap, S. Mutual Coupling Reduction of Microstrip MIMO Antenna Using Microstrip Resonator. *Wirel. Pers. Commun.* **2020**, *112*, 2047–2056. [CrossRef]
15. Pasumarthi, S.R.; Kamili, J.B.; Avala, M.P. Design of Tri-Band MIMO Antenna with Improved Isolation using DGS and Vias. *Wirel. Pers. Commun.* **2019**, *110*, 1523–1532. [CrossRef]
16. Hasan, N.; Chu, S.; Bashir, S. A DGS monopole antenna loaded with U–shape stub for UWB MIMO applications. *Microw. Opt. Technol. Lett.* **2019**, *61*, 2141–2149. [CrossRef]
17. Tiwari, R.N.; Singh, P.; Kanaujia, B.; Srivastava, K. Neutralization technique based two and four port high isolation MIMO antennas for UWB communication. *AEU-Int. J. Electron. Commun.* **2019**, *110*, 152828. [CrossRef]
18. Gomez-Villanueva, R.; Jardon-Aguilar, H. Compact UWB Uniplanar Four-Port MIMO Antenna Array With Rejecting Band. *IEEE Antennas Wirel. Propag. Lett.* **2019**, *18*, 2543–2547. [CrossRef]
19. Hassan, M.M.; Rasool, M.; Asghar, M.U.; Zahid, Z.; Khan, A.A.; Rashid, I.; Rauf, A.; Bhatti, F.A. A novel UWB MIMO antenna array with band notch characteristics using parasitic decoupler. *J. Electromagn. Waves Appl.* **2019**, *34*, 1225–1238. [CrossRef]
20. Liu, H.; Kang, G.; Jiang, S. Compact Dual Band–Notched Uwb Multiple–Input Multiple–Output Antenna for Portable Applications. *Microw. Opt. Technol. Lett.* **2020**, *62*, 1215–1221. [CrossRef]
21. Tang, Z.; Zhan, J.; Wu, X.; Xi, Z.; Wu, S. Simple Ultra–Wider–Bandwidth Mimo Antenna Integrated by Double Decoupling Branches and Square–Ring Ground Structure. *Microw. Opt. Technol. Lett.* **2019**, *62*, 1259–1266. [CrossRef]
22. Kumar, S.; Lee, G.H.; Kim, D.H.; Mohyuddin, W.; Choi, H.C.; Kim, K.W. Multiple–Input–Multiple–Output/Diversity Antenna with Dual Band–Notched Characteristics for Ultra–Wideband Applications. *Microw. Opt. Technol. Lett.* **2019**, *62*, 336–345. [CrossRef]
23. Raheja, D.K.; Kanaujia, B.K.; Kumar, S. Low Profile Four–Port Super–Wideband Multiple–Input–Multiple–Output Antenna with Triple Band Rejection Characteristics. *Int. J. RF Microw. Comput.-Aided Eng.* **2019**, *29*, e21831. [CrossRef]
24. Wani, Z.; Kumar, D. A Compact 4 × 4 Mimo Antenna for Uwb Applications. *Microw. Opt. Technol. Lett.* **2016**, *58*, 1433–1436. [CrossRef]

25. Sipal, D.; Abegaonkar, M.P.; Koul, S.K. Compact Planar 2 × 2 and 4 × 4 Uwb Mimo Antenna Arrays for Portable Wireless Devices. *Microw. Opt. Technol. Lett.* **2018**, *60*, 86–92. [CrossRef]

26. Kan, G.; Lin, W.; Liu, C.; Zou, D. An array antenna based on coplanar parasitic patch structure. *Microw. Opt. Technol. Lett.* **2018**, *60*, 1016–1023. [CrossRef]

27. Yang, B.; Chen, M.; Li, L. Design of a four-element WLAN/LTE/UWB MIMO antenna using half-slot structure. *AEU-Int. J. Electron. Commun.* **2018**, *93*, 354–359. [CrossRef]

28. Ali, W.A.; Ibrahim, A.A. A compact double-sided MIMO antenna with an improved isolation for UWB applications. *AEU-Int. J. Electron. Commun.* **2017**, *82*, 7–13. [CrossRef]

29. Shehata, M.; Said, M.S.; Mostafa, H. Dual Notched Band Quad-Element MIMO Antenna With Multitone Interference Suppression for IR-UWB Wireless Applications. *IEEE Trans. Antennas Propag.* **2018**, *66*, 5737–5746. [CrossRef]

30. Mathur, R.; Dwari, S. Compact CPW-Fed ultrawideband MIMO antenna using hexagonal ring monopole antenna elements. *AEU-Int. J. Electron. Commun.* **2018**, *93*, 1–6. [CrossRef]

31. Dhasarathan, V.; Nguyen, T.K.; Sharma, M.; Patel, S.K.; Mittal, S.K.; Pandian, M.T. Design, Analysis and Characterization of Four Port Multiple-Input-Multiple-Output Uwb-X Band Antenna with Band Rejection Ability for Wireless Network Applications. *Wirel. Netw.* **2020**, *26*, 4287–4302. [CrossRef]

32. Addepalli, T.; Anitha, V.R. Design and analysis of a novel compact spanner-shaped ultra-wideband antenna for MIMO systems. *Int. J. Commun. Syst.* **2021**, 1–13. [CrossRef]

33. Liu, L.; Cheung, S.W.; Yuk, T.I. Compact Multiple–Input–Multiple–Output Antenna Using Quasi–Self–Complementary Antenna Structures for Ultrawideband Applications. *IET Microw. Antennas Propag.* **2014**, *8*, 1021–1029. [CrossRef]

34. Jafri, S.I.; Saleem, R.; Shafique, M.F.; Brown, A.K. Compact Reconfigurable Multiple–Input–Multiple–Output Antenna for Ultra Wideband Applications. *IET Microw. Antennas Propag.* **2016**, *10*, 413–419. [CrossRef]

35. Boukarkar, A.; Lin, X.Q. Miniaturized Frequency–Tunable Self–Quadruplexing Four–Element Mimo Antenna System. *IET Microw. Antennas Propag.* **2020**, *14*, 973–979. [CrossRef]

36. Kumar, P.; Urooj, S.; Alrowais, F. Design of Quad-port MIMO/Diversity Antenna with Triple-band Elimination Characteristics with Super-widenband Applications. *Sensors* **2020**, *20*, 624. [CrossRef]

37. Kumar, P.; Urooj, S.; Malibari, A. Design of Quad-Port Ultra-Wideband Multiple-Input-Multiple-Output Antenna with Wide Axial-Ratio Bandwidth. *Sensors* **2020**, *20*, 1174. [CrossRef]

38. Yin, W.; Chen, S.; Chang, J.; Li, C.; Khamas, S. CPW Fed Compact UWB 4-Element MIMO Antenna with High Isolation. *Sensors* **2021**, *21*, 2688. [CrossRef]

39. Alsaif, H.; Eleiwa, A.H. Compact Design of 2×2 MIMO Antenna with Super-Wide Bandwidth for Millimeters Wavelength Systems. *Symmetry* **2021**, *13*, 233. [CrossRef]

40. Sharma, M.; Vashist, P.C.; Ashtankar, P.S.; Mittal, S.K. Compact 2×2/4×4 tapered Microstrip feed MIMO Antenna configuration for gigh-speed wireless applications with band stop filters. *Int. J. RF Microw. Comput.-Aided Eng.* **2020**, *31*, e22500.

41. Sharma, M.; Awasthi, Y.K.; Singh, H. Design of CPW-fed High Rejection Triple Band-Notch UWB Antenna on Silicon with Diverse wireless applications. *Prog. Electromagn. Res. C* **2017**, *74*, 19–30. [CrossRef]

42. Balanis, C.A. *Antenna Theory: Analysis and Design*, 4th ed.; Wiley Publication: Hoboken, NJ, USA, 2016.